Impulse saturation in metal plates under confined blasts

Ye Yuan[1,2*], Xudong Li[3], Chengjian Zhang[1,2], P.J. Tan[4], Pengwan Chen[1,2*]

[1] *State Key Laboratory of Explosion Science and Technology, Beijing Institute of Technology, Beijing 100081, PR China*

[2] *Explosion Protection and Emergency Disposal Technology Engineering Research Center, Ministry of Education, PR China*

[3] *North University of China, Taiyuan 030051, Shanxi, PR China*

[4] *Department of Mechanical Engineering, University College London, Torrington Place, London WC1E 7JE, UK*

Abstract

The phenomenon of impulse saturation is revisited for metal plates subjected to confined blasts through a combination of experiments, numerical simulations, and analytical modeling. Internal blast experiments were performed on the fully-clamped aluminium square plate where its transient inelastic (mode I) response was recorded using three-dimensional digital image correlation (DIC). A methodology was proposed to idealise the confined blast induced pulse-pressure through a validated numerical model. An analytical model was developed to predict the transient central deflection of the aluminium plate under the idealised pulse pressure, where the predictions were shown to be in reasonable agreement with the DIC measurements. Parametric studies were performed to elucidate the effect of standoff distance and confinement geometry on the saturation duration, saturated impulse and deflection. It was found that both the pulse-shape and saturated impulse strongly influence the saturated deflection during internal blast loadings.

Keywords: Internal blast loading, Impulse saturation, Large deformation, Blast experiments, Modelling

1. Introduction

There have been growing interests on impulse saturation phenomenon recently [1–3]. It is a peculiar phenomenon associated with irreversible deformation of ductile structures subjected

*Corresponding author

Email addresses: yuanye20@bit.edu.cn (Ye Yuan[1,2]), pwchen@bit.edu.cn (Pengwan Chen[1,2])

to blast loadings. Under pulse-pressure loading of a sufficiently long duration, the transverse deflection of a metal plate cannot increase indefinitely without bound, but reaches a maximum at a certain time referred to, hereinafter, as the *saturation time*. In other words, only the impulse transmitted during the early part of a long pulse-pressure contributes to the final, maximum out-of-plane deflection (known, alternatively, as the *saturated deflection*) of the plate. Beyond this saturation time, any further impulse transmitted does not lead to an increase in its maximum out-of-plane deflection. The physical explanation is that the load-bearing capacity of the structure is enhanced by the membrane force induced by its large deflection and could resist the external load acting on it. Although this phenomenon is absent for impulsive loading scenarios where loading duration is infinitesimally short, it is inevitable, and quite pertinent, for blast loadings with considerable durations such as far-field air blasts and confined blast loadings.

There exists a large body of literature that deals with the analytical investigations of impulse saturation based on the framework of limit analysis [1, 2, 4–10]. Early studies by Jones [4] reported the phenomenon that under rectangular or triangular pulse-pressure of a sufficiently long duration, a plate structure reaches its maximum transverse deflection well before the end of the pressure pulse, and this permanent deflection remains unchanged despite continued loading by the pressure pulse. After Zhao [5, 6] defined the terminology 'impulse saturation' and investigated this phenomenon for rigid perfectly-plastic beams under rectangular pulse pressure, the term impulse saturation phenomenon has been widely used. In recent years, Zhu, Yu et al. [2, 7–9] systematically carried out saturation analysis for pulse-loaded beams and plates. Their analytical model has been evolving to be more accurate and comprehensive, i.e., many features have been considered over the years, such as the effect of travelling plastic hinge lines [2], effects of strain rate sensitivity and strain hardening [8], the effect of boundary condition [7], and arbitrary pulse shape [9]. Yuan et al. [3], on the other hand, employed an elasto-plastic analytical model [10] to study the impulse saturation for a fully clamped beam under blast loading. Besides beams and plates, Karagiozova and Alves [1] recently found that the impulse saturation phenomenon may occur in a hollow beam with a circular cross-section under a uniformly distributed rectangular pressure pulse loading.

One possible application of the aforementioned saturation analysis lies in the field of confined blast loaded metal plates. Confined blast loading, compared to its free-field counterpart, is more complex and destructive due to the multiple shock wave reverberating within the confinement [11]. Although the confined pulse-pressure loading may be influenced by many factors such as confinement geometry [12, 13], charge mass [14], standoff distance [15], the extent of venting [16, 17] and the degree of confinement [18], the common distinctive features are the amplified peak overpressure, the multiple spikes in its pulse shape and the significant period of quasi-static loading. Undoubtedly, the total impulse from a confined blast loading is significant as a result of the considerable loading period. However, it does not necessarily represent the effective impulse (or the impulse saturation) that leads to a metal structure's maximum transverse displacement. The significance of the impulse saturation phenomenon in confined blast loaded square plates has been recently recognised by Yuan et al. [15]

who studied the effect of standoff distance in confined blasts through experiments and finite element simulations. They found that the impulse saturation phenomenon contributes to the interesting finding that a greater standoff distance would lead to a higher saturated deflection, and the saturated deflection at different standoff distances is proportional to its saturated impulse, instead of the total one.

Hitherto, a thorough investigation of the impulse saturation phenomenon in confined blast cases is still lacking. The existing saturation analysis (e.g. [2, 8, 9, 19]) – though the predictions of which agree well with corresponding numerical one – has not been validated by experiments. The current study carries out a combined experimental, numerical and analytical study to investigate the dynamic response of aluminum plate under confined blast loading. The aluminum plate was loaded by internal blast loadings from the detonation of cylindrical 8701 charges within a stiff blast chamber. A methodology will be proposed to combine the numerical and analytical simulations to address the internal blast loading idealisation and structural response, respectively. Numerical simulations were performed to acquire the average interface overpressure acting on the structure that would serve as the external loading condition for the analytical model. Analytical investigations, based on a modified model of the authors' previous work [20], were carried out to estimate the transient transverse deflection of the square plate under confined blast loadings. The analytical model will be used to carry out parametric studies to investigate the effect of standoff distance and confinement geometry upon the saturation time, saturated impulse and deflection. The model developed in this work should also be useful to blast engineers seeking quick and accurate predictions of the transient deflection of ductile structures under internal blast loading (e.g. uniform pulse pressure generated by detonating an explosive charge at the end of a square tunnel) in the preliminary design stage.

2. Experiments

2.1. Setup

Figure 1 shows a schematic of the experimental setup. The test rig consisted of a 'stiff' blast chamber, a rigid blanking plate, flange and plate specimen, see Fig. 1a. The blast chamber has dimensions of 0.4 m × 0.4 m × 0.8 m with a square opening of 0.3 × 0.3 m at opposite ends. The chamber walls were constructed from 0.01 m thick Q235 steel plates with reinforced ribs that can withstand multiple internal blasts. The entire chamber was placed on the top of a metal supporting frame, as shown in Fig. 1d. To restrain any global motion during the blast test, the supporting frame was welded to the metallic floor and the blast chamber was welded to the supporting frame. The plate specimens with the in-plane dimension of 0.4 m × 0.4 m × 0.002 m were peripherally clamped between the flange and the support frame of the blast chamber through 12 M20 bolts. The other end of the blast chamber was sealed by clamping a 0.01 m thick steel blanking plate in the same fashion. There was a ϕ60 mm venting hole at the top of the blast chamber to allow fast dissipation of the quasi-static pressure from the confined blast loading. The confined blast loading was generated from the detonation of a cylindrical 8701 explosive, which was suspended from the

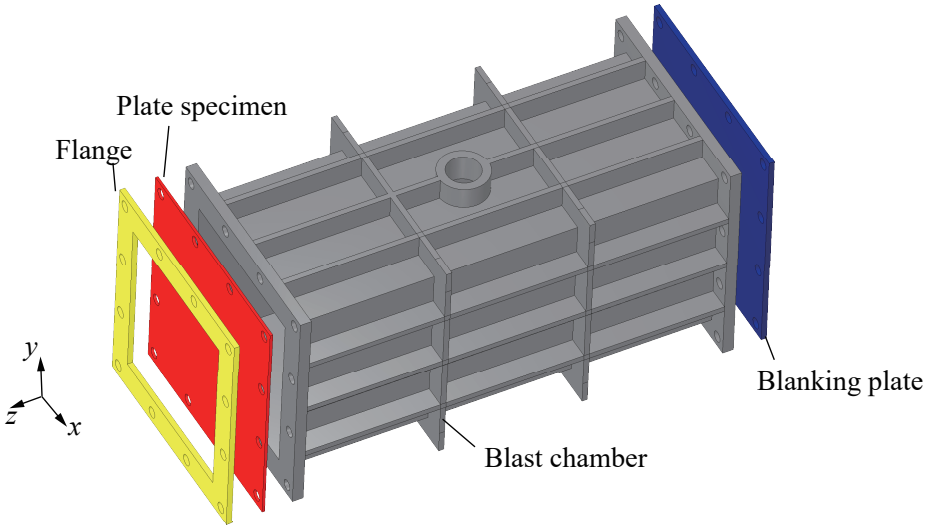

(a) Schematic of the test rig

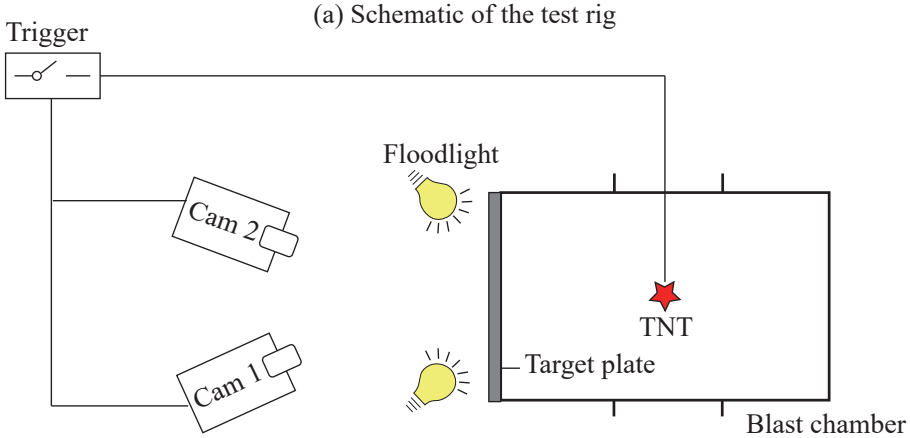

(b) Experimental setup

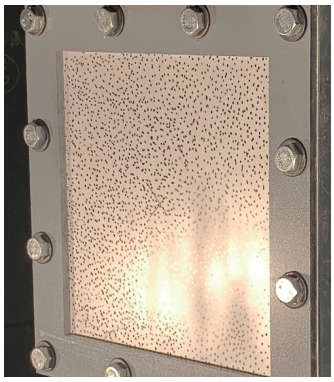

(c) DIC speckle pattern

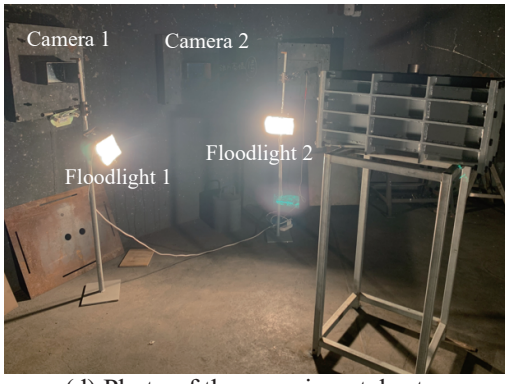

(d) Photo of the experimental setup

Figure 1: Schematic of the experimental setup to perform the internal blast loading experiment.

venting hole. The accurate vertical position of the explosive ($y-$direction in Fig. 1a) was ensured such that the line connecting the centroid of the plate specimen to the center of the

explosive remains perpendicular to the exposed surface of the plate specimen. The center of the explosive also coincided to that of the blast chamber, keeping a constant standoff distance – between the plate specimen and the explosive – of 0.4 m through out the current tests. In total, only one blast test was carried out. Since the primary interest of the current work lies in the metal plate's elasto-plastic deformation, instead of ductile failure, a low level of charge mass, i.e., 10g, was used. The experimental results on elasto-plastic deformation will be used to validate the proposed numerical and analytical predictions (to be presented later).

The three-dimensional digital image correlation (3D DIC) technique was used to measure the plate specimen's transient evolution of full-field deformation. Two Photron FASTCAM SA5 high-speed cameras were placed in a symmetric stereo-imaging setup as shown in Fig. 1b. Both cameras were operated at 30000 frames per second (fps), producing an image resolution of 448 $\times$ 448 pixels. To enable the image correlation algorithm to track the plate surface, white background, and stochastic black speckle pattern were applied to the plate surface as shown in Fig. 1c. Two floodlights were used to provide additional lighting for the speckle pattern to have enough contrast to calculate the transient deformation fields using DIC, as shown in Fig. 1d.

Before performing the blast test, the stereovision system is calibrated using a target with the in-plane dimension of 0.5 $\times$ 0.5 m applied with a dot grid pattern. During calibration, 25 images of the target (tilted and rotated into different orientations), were acquired to generate the necessary spatial data. They were used to determine the intrinsic (e.g. image center) and extrinsic (e.g. orientation of each camera relative to target) camera parameters, including correction of radial and tangential lens distortion through optimisation for each of the two cameras. The high-speed cameras were synchronised and triggered together with the triggering of the 8701 detonation. The recorded images were post-processed to generate the transient out-of-plane displacement field of the plate specimen.

2.2. Material

Quasi-static tests were carried out to characterise the constitutive behaviour of 6061 aluminum (6061 Al). Uniaxial tensile tests were conducted in an Instron 5982 universal testing machine with a 100 kN load cell at an initial strain rate of 5 $\times$ 10^{-4} s^{-1}. The nominal stress-strain curves in the uniaxial quasi-static tensile test is shown in Fig. 2. The data in Fig. 2 would be used to calibrate the Johnson-Cook parameters associated with linear hardening effect later in section 3.1.

2.3. Results

Figures 3 shows the experimental result of the aluminum plate's transverse displacements obtained from the DIC measurements at four selected time instants. Note that time $t = 0$ ms refers to the instant when there is a non-zero transverse central displacement, instead of the detonation time. The four deflection incidences correspond to the typical stages of initial response, elasto-plastic deformation, maximum deflection, elastic rebound. The left columns present the evolution of the transverse displacement distribution. The deformation field is

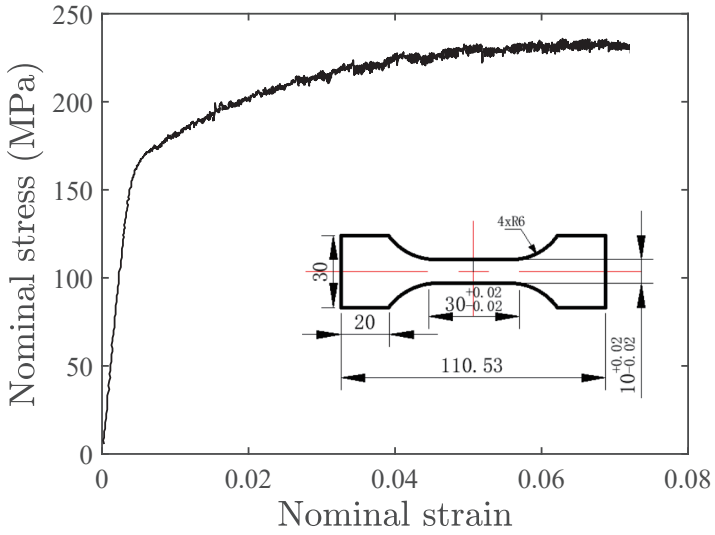

Figure 2: Quasi-static nominal stress-strain curves for the 6061 alumimum materials used in this work.

Table 1: Summary of the confined blast test.

Saturation time (ms)			Maximum central displacement (mm)			Permanent central displacement (mm)		
Exp	FE	Analytical	Exp	FE	Analytical	Exp	FE	Analytical
0.77	0.58	0.74	22.97	21.16	23.80	21.8	18.50	23.80

not strictly symmetrical about the y-axis at $x = 0$, and is slightly offset to the positive x-axis. This may be due to the misalignment of the explosive in the experiment such that the loading was more intensive towards the right half of the target plate. Notwithstanding the deformation profiles were quite symmetrical about the $x-$axis at $y = 0$, as indicated in the lengthwise deformation profiles in the middle column of Fig 3. Despite the slight asymmetry in deformation, the plate's response was still characterised by its foundamental modes of vibration. The evolution of the plate profile is reminiscent of a typical blast-loaded square plate [21]. For example, there is a sharp rise and a subsequent flattening in the central region (as a result of the plastic hinge lines formation) at early response stages (first two deflection incidences) followed by an overall dome shape at later response stages (last two deflection incidences).

The maximum transient deflection of the entire plate was extracted from the DIC measurements, and was plotted in the right column of Figures 3. Due to the aforementioned asymmetry in response, the maximum deflection was not attained at the plate centre. The central deflection is 9.6% less than the maximum one. The plate displayed typical elasto-plastic responses consisting of an initial sharp rise to a maximum value followed by a periodic elastic rebound. From the entire time history of the transverse central displacement, one can

read off the maximum transverse displacement and the passage of time from when the displacement is above zero to the time when the maximum transverse displacement is attained. In the case of the confined blast where the loading duration is significant, it is reasonable to postulate that this passage of time is the saturation time t_{Sat} – the numerical simulations (to be shown in Section 3.3) will confirm this. The characteristics of the confined blast tests, including the saturation time, maximum and permanent central displacements, are tabulated in Table 1. Although the corresponding finite element and analytical predictions are also available in Table 1, they will not be discussed until later in Section 3.2 and 4.4.

3. Numerical simulations

The numerical simulations aim to obtain the time history of the blast loading acting on the target plate in the confined blast test, which was not recorded during the experiment. An accurate description of the loading condition is of paramount importance to achieving successful analytical modeling of the current problem. This section will present the development of the numerical model, its validation against experimental results, and the methodology to idealise the internal blast loadings.

3.1. Numerical model

The numerical model was developed using the commercial code, ANSYS/LS-DYNA® 2020. To capture the fluid-structure (internal blast wave and plate specimens) interaction, the coupled Eulerian-Lagrangian approach was used. Figure 4 shows that the numerical model consists of air, explosives, the blast chamber, the blanking plate and the plate specimen. The air and explosives were discretised by Eulerian eight-noded brick elements, and the rest of the components are by Lagrangian four-noded shell elements. A penalty coupling technique was employed to enforce the fluid-structure interaction. It is noteworthy that the air extended beyond the blast chamber, covering the plate specimens' rear to account for their deformations. The Euler domain had the dimension of $0.25 \times 0.5 \times 1.25$ m. A 'flow-out boundary' condition was used to allow the gas product to dissipate beyond the Euler domain. Only half of the model was needed to be simulated, taking the advantage of the symmetry. Instead of modelling a realistic boundary condition including the bolts, the flange, and their contact, the plate specimen was fully clamped along its periphery that is outside the exposed loading area. Although adopting this idealisation would neglect the movement of the flange and the plate specimen around the bolts, its impact on the fidelity of the current numerical prediction of the plate deformation is considered to be minor, since no notable elongation at the holes was found after the tests. The walls of the blast chamber and the blanking plate were modeled as rigid material [14, 22]. A mesh convergence study was carried out to analyse the sensitivity of predictions of plate displacement to the Eulerian and Lagrangian elements, following the procedure outlined in the authors' previous study [15]. The mesh sensitivity study showed that a mesh size of 0.005 m in the air domain is adequate to predict the development of internal blast loading with excellent fidelity, and a uniform 0.004×0.004 m^2 mesh was refined enough to predict the deflection with reasonable accuracy.

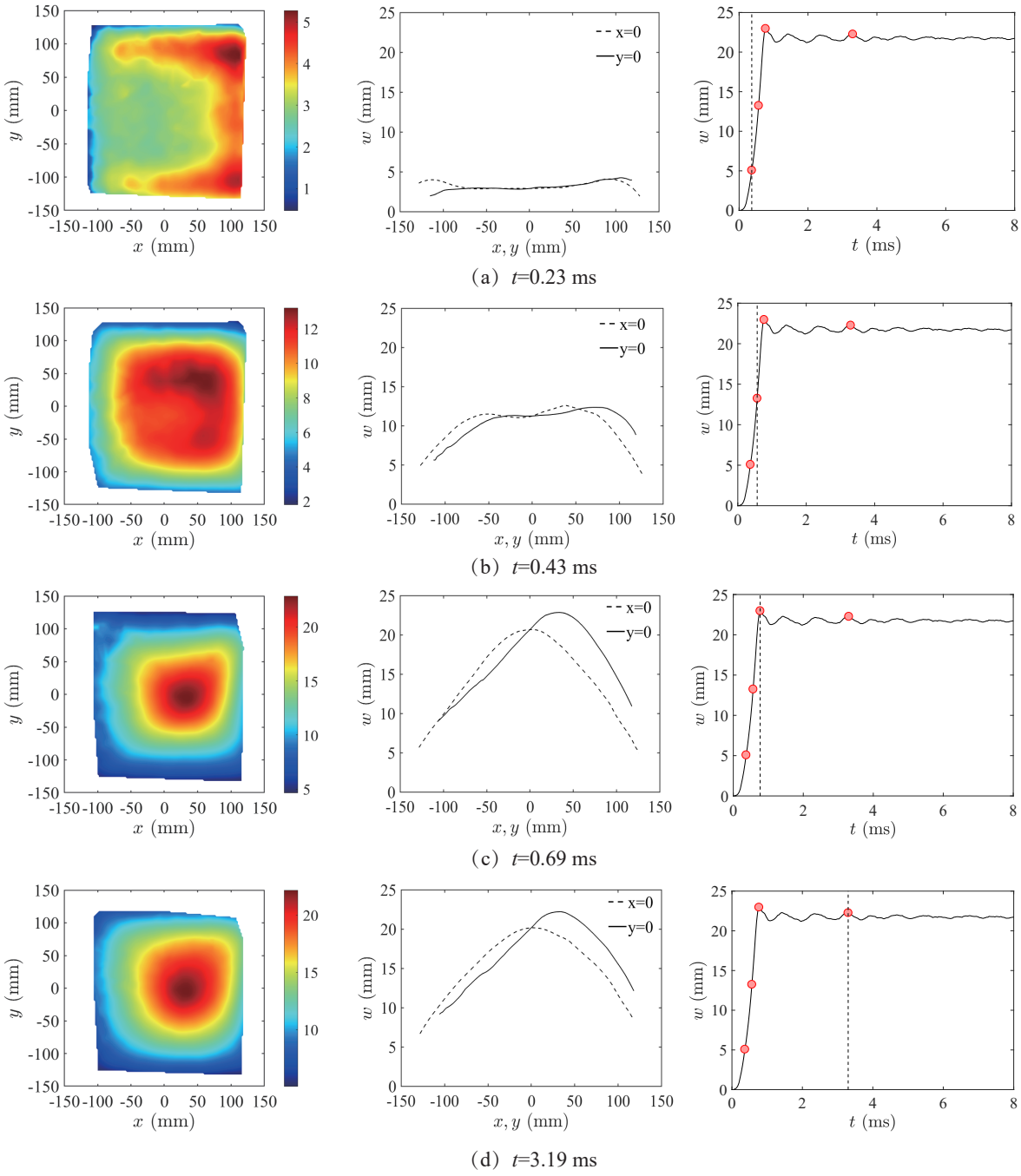

Figure 3: Experimental results at selected time instants: transverse displacement contour extracted from DIC image (left), deformation profile in the plate centre along x and y axis (middle), and entire time-history of the ~~midpoint displacement~~transverse deflection (right).

The air was modeled as a null material obeying the ideal gas law. Standard air properties – the specific heat ratio γ_a, air density ρ_a, internal energy e_a and initial air pressure p_a – are used, which are given in Table. 2. The explosive was modeled using the Jones-Wilkins-Lee

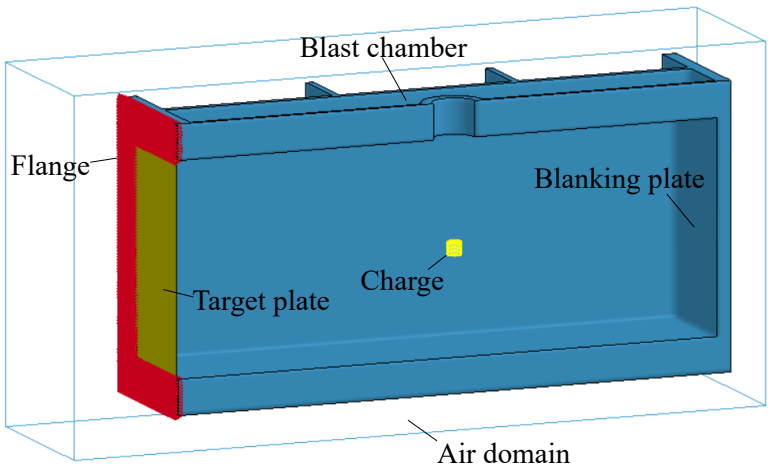

Figure 4: Schematic of the numerical model of one half of the fully clamped square plate subjected to internal blast loading.

(JWL) EOS (or the high-explosive burn material model in LS-DYNA). The EOS parameters had the non-dimensional terms (r_1, r_2 and ω) and the pressure terms (C_1 and C_2). The detonation parameters comprised of initial density of the explosive ρ_0, the Chapman-Jouguet pressure P_{CJ} and the detonation velocity D. The values for the aforesaid parameters used for 8701 were given in Table 3.

Table 2: The properties of air used in the present simulations.

ρ_a (kg/m^3)	e_a (KJ/Kg)	p_a (Pa)	γ_a
1.225	206.8	104761	1.4

Table 3: The properties of the explosives used in the simulations.

ρ_0 (kg/m^3)	D (m/s)	P_{CJ} (GPa)	a (GPa)	b (GPa)	r_1	r_2	ω
1710	8315	28.60	524.23	7.68	4.20	1.10	0.34

A modified Johnson-Cook with Cowper-Symonds overstress power law was used to describe the plate's constitutive behaviour. It relates the Von Mises equivalent flow stress σ to the equivalent plastic strain ϵ, strain rate $\dot{\epsilon}$ and temperature T through

$$\sigma = (A + B\epsilon_p^n)(1 + \left|\frac{\dot{\epsilon}}{\dot{\epsilon}_0}\right|^{1/q})(1 - T^{*m}) \tag{1}$$

where A is the static yield stress, B is the strain hardening coefficient, n is the strain hardening exponent, $\dot{\epsilon}_0$ and q are the strain rate sensitivity coefficient, $T^* = (T-T_r)/(T-T_m)$ is the homologous temperature, T_r is the reference temperature, T_m is the melt temperature and m is the thermal sensitivity exponent. Collectively, the terms within the first and second brackets of Eq. 1 correspond to the strain hardening and strain rate dependency of the material model at room temperature, respectively. The stress-strain curve in Fig. 2 was used to obtain the model parameters (those within the first bracket of Eq. 1) via linear fitting. No additional characterisation tests were performed to obtain the rate-dependency and thermal softening parameters. Instead, they were taken from published literature [23, 24]. The parameters of the JC model were tabulated in Table 4 and the physical constants for 6061 aluminum – extracted from literature [25] – were listed in Table 5.

Table 4: Parameters used in the modified Johnson-Cook (JC) constitutive model.

Material	A (MPa)	B (MPa)	n	$\dot{\epsilon}_0$ (1/s)	q	m
6061 Al	173	369.8	0.5542	6500 [23]	4 [23]	1 [24]

Table 5: Physical properties for the material from literature.

Material	E (GPa)	ν	ρ kg/m^3
6061 Al [25]	64	0.33	2700

3.2. Validations

In this subsection, the FE predictions are validated against the experimental data. Figure 5 shows that the time-history of maximum deflection is in reasonable agreement with the 3D-DIC measurement. The FE model seems to slightly underpredicts the saturated deflection (7.9 %) and overpredicts the saturation time (11.6 %) compared to the experimental counterparts (as also noted in Table 1)). The prediction of deformation profile along $x-$ and $y-$axis at selected time instants are compared against the 3D-DIC measurements in Fig. 6. Although good agreements can be seen in Fig. 6b, there is notable discrepencies in Fig. 6a that is due to the asymmetry response in the experiment.

3.3. Idealised internal blast loading

This subsection proposes a methodology to idealise the overpressure acting on the target structure under the confined blast. To this end, it is important to first understand the evolution of the pressure field in the confined blast event. Figure 7 unfolds the evolution of the pressure distribution within the air domain at selected time instants. Notice that $t = 0$ ms corresponds to blast wave arrival time and negative t indicates the scenario that the blast

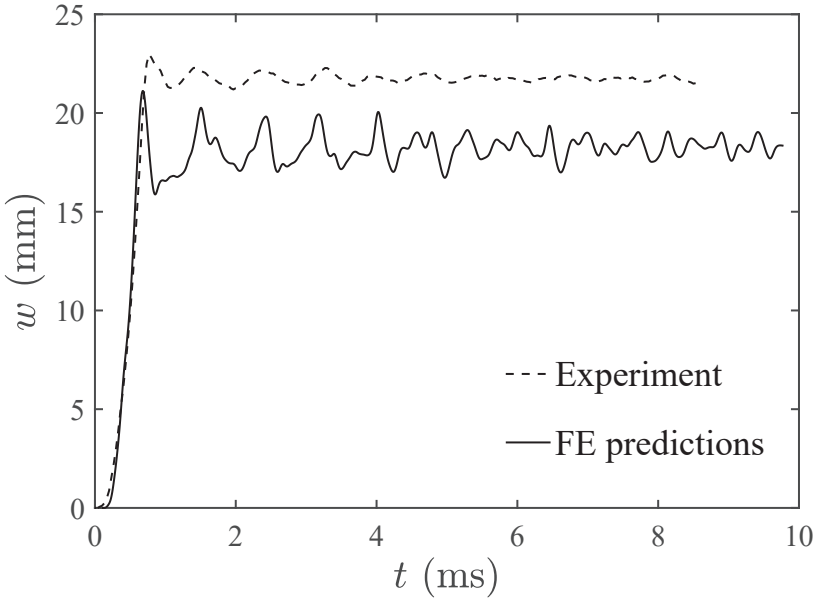

Figure 5: Comparison of the numerical temporal central displacement with experimental data for the aluminum plate.

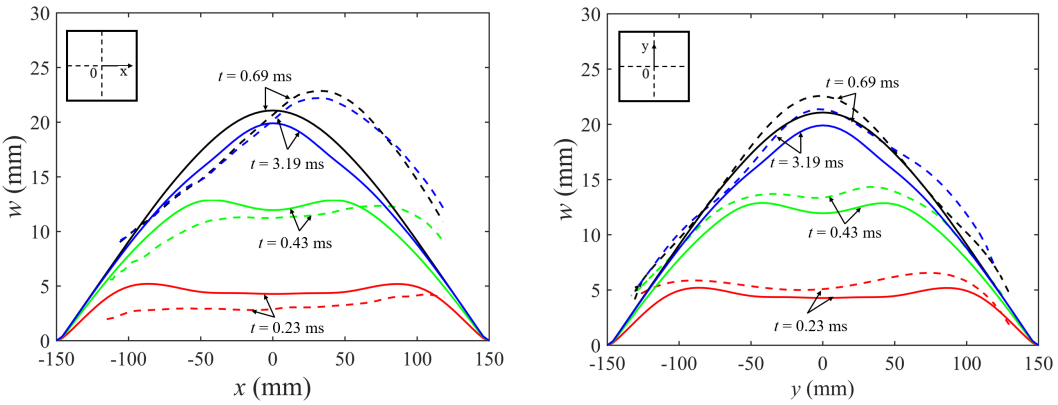

(a) $y = 0$ (b) $x = 0$

Figure 6: Comparison of the predicted lengthwise deformation profile and experimental results for the aluminum plate at different time instants. Solid lines — and dotted lines - - - refer to the FE and experimental results respectively.

wave has not reached the target plate. The blast wave was initially spherical after detonation ($t = -0.3$ ms), and started to interact with the adjacent walls ($t = -0.25$ ms), with pressure partly vented through the opening hole at the top. The blast wave finally reached the target plate at $t = 0.0$ ms, after which instant the blast wave immediately got reflected backward traveling towards the opposite ends. This reflected blast wave somehow met another blast wave traveling in the opposite direction, in the midpoint of the chamber (t=0.45 ms) and

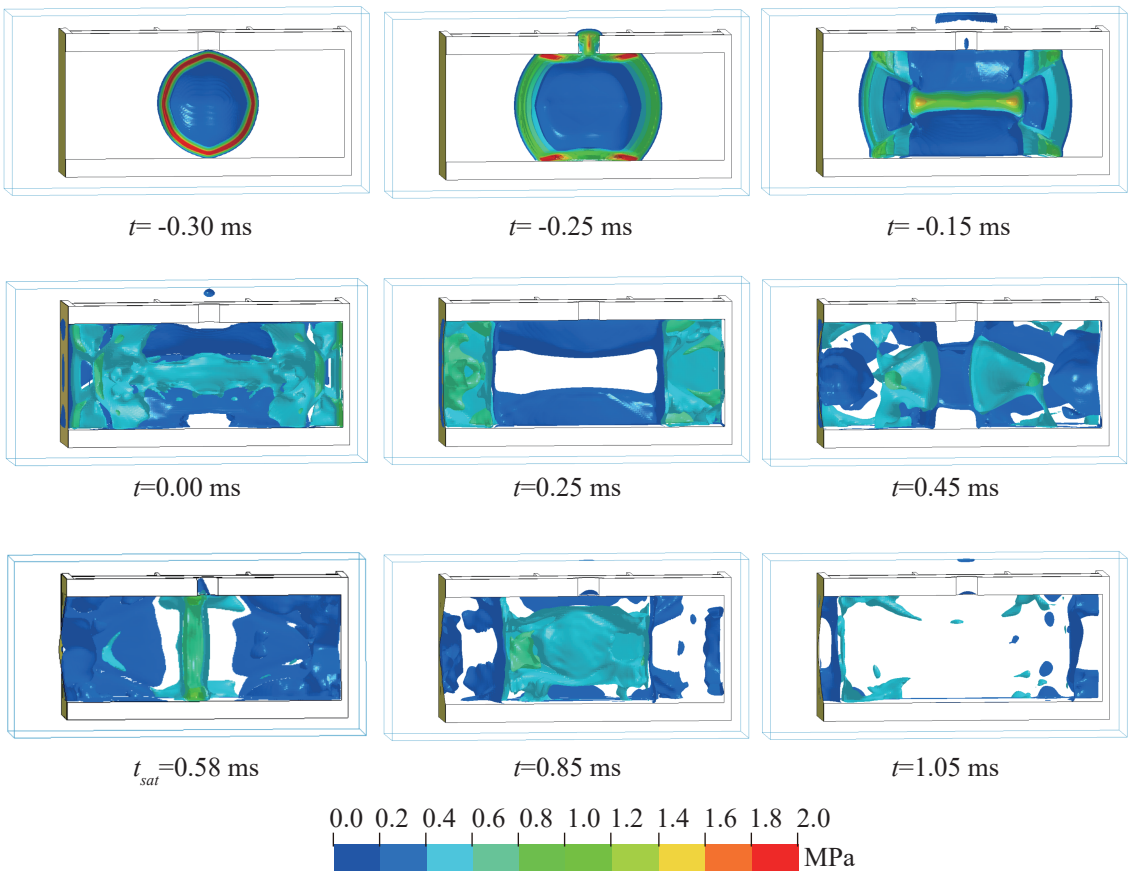

Figure 7: Temporal evolution of the pressure wave generated by a 10g of 8701 charge and its interaction with the aluminum plate. Note here that $t = -0.30$ ms refers to the time instant after 0.05 ms of explosive detonation.

inevitably causing another round of reverberation. The constant wave reflections, with a certain interval in-between, were the intrinsic characteristics of internal blast loading [15]. It is worth highlighting that the 3D pressure field was initially almost symmetrical about the mid planes of the blast chamber before the target plate developed large elastoplastic deformation (at $t = 0.45$ ms), resulting in fluid-structure interaction effects that affect the subsequent pressure field.

Given that the saturated deflection was reached at $t = 0.58$ ms, it is reasonable to postulate that the primary blast wave was responsible for the plates' maximum response and the subsequent loading was unable to cause any additional central deflection. Between $t = 0 - 0.65$ ms, the contour of the overpressure acting on the exposed area of the target plate was shown in Fig. 8. It is interesting to notice that the pressure, upon arrival, was first concentrated at the four corners of the plate's exposed area ($t = 0.0$ ms) before spreading to the rest of the plate in a uniform fashion from $t = 0.05 - 0.1$ ms, and gradually disappeared with the passage of time from $t = 0.15 - 0.65$ ms. After the saturation time of 0.58 ms, the intensity of the loading drops significantly. Evident is the non-uniform characteristic of the

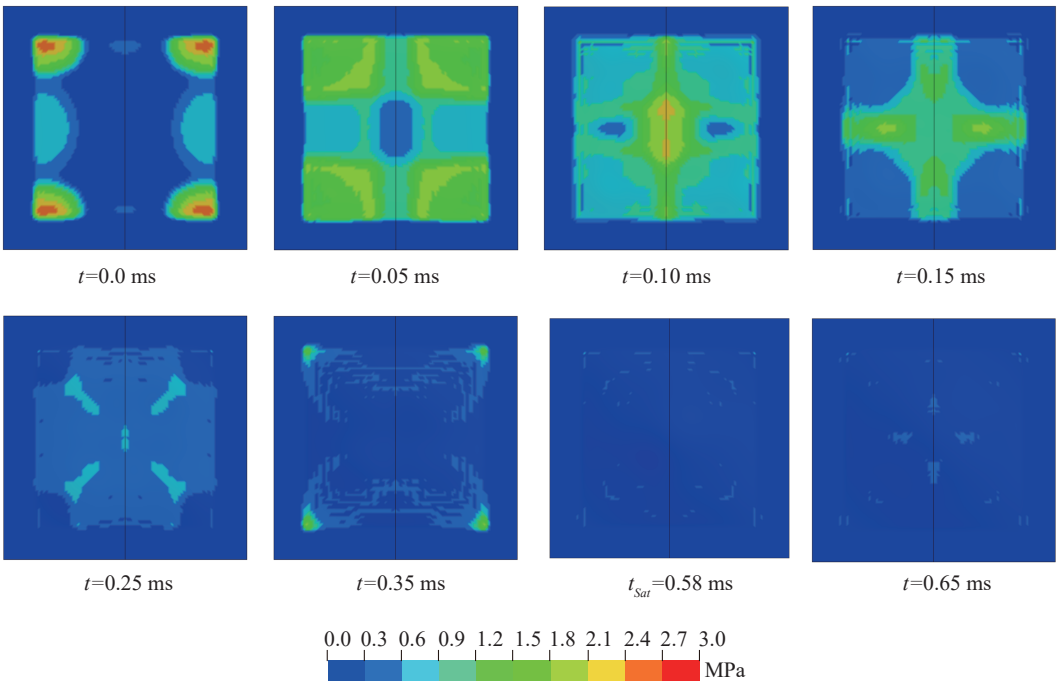

Figure 8: Evolution of overpressure distribution acting on the aluminum plate.

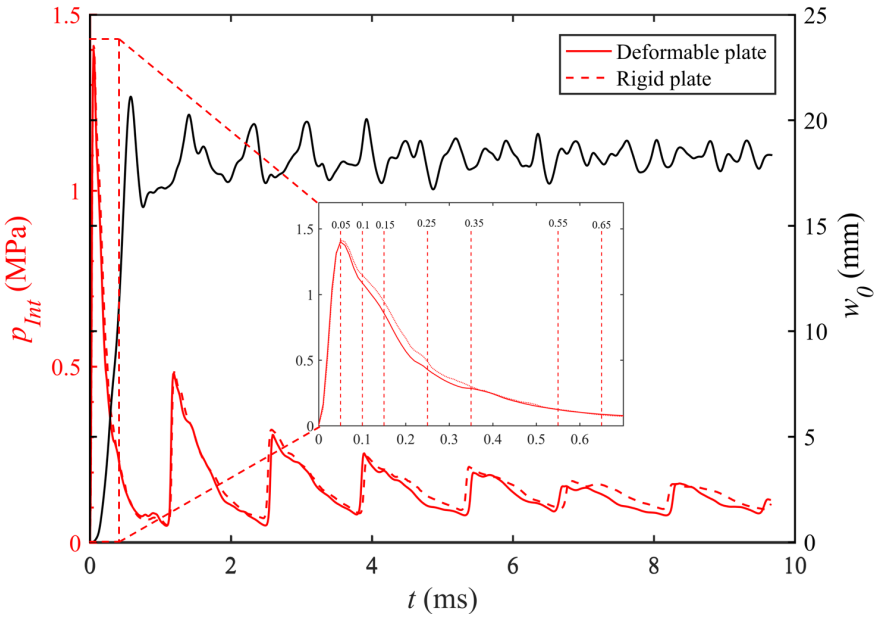

Figure 9: Comparison of the numerical predictions of average interface overpressure on the exposed surface for the deformable aluminum plate $p_{\text{Int}}^{\text{Def}}$ (— red solid line) and the rigid plate $p_{\text{Int}}^{\text{Rigid}}$ (- - - red dotted line). The selected time instants in Fig. 8 are marked in the magnified region. The predicted transient deflection of the deformable plate (— black solid line) is also superimposed in this figure.

loading distribution during the structural deformation up to its maximum response.

To quantify the internal blast loading experienced by the plate, the interface overpressure off the deformable plate was extracted from the FE simulation results. The time-history of the *average* interface overpressure on the deformable plate was shown in Fig. 9. The predicted transient deflection is also plotted here to indicate the significance of the saturation phenomenon. It is clear that the the saturation time (t_{Sat} =0.58 ms) is much smaller compared to the loading duration. The curve of the average interface overpressure resembles the characteristics of a typical internal blast loading, viz. a primary blast wave following by multiple spikes with decreasing amplitude. To achieve a quick estimation of the consequence of a blast loading, the complex interaction between the blast wave and the structure are often neglected by blast protection designer to permit a decoupled analysis where a given pulse-pressure (with a certain pulse-profile) is directly applied to the target structure. In light of this, a separate simulation was carried out with identical numerical settings apart from substituting the aluminum plate with a rigid plate. The prediction of the average interface overpressure off the rigid plate was plotted in Fig. 9 (in dotted line) for comparison. Comparing the interface overpressure from a deformable plate $p_{\text{Int}}^{\text{Def}}$ and from a rigid plate $p_{\text{Int}}^{\text{Rigid}}$ is also a common practice to reveal the significance of the FSI effect [26–28], and the case of $p_{\text{Int}}^{\text{Rigid}}$ represents the extreme case of non-FSI effect (or the theoretical upper bound of $p_{\text{Int}}^{\text{Def}}$). It can be seen that the two curves are almost indiscernible at initial stage ($t = 0 - 6$) ms, but start to have notable discrepancy in later stage ($t = 0.65 - 10$ ms); and $p_{\text{Int}}^{\text{Rigid}}$ is also always marginally greater than $p_{\text{Int}}^{\text{Def}}$, as expected, indicating the extent of overprediction if ignoring FSI.

To investigate whether the above averaged interface overpressures ($p_{\text{Int}}^{\text{Def}}$ and $p_{\text{Int}}^{\text{Rigid}}$) can be served as accurate representations of the actual internal blast loading for the target plate, those loadings were applied directed to the target plate as uniformly distributed pressure, in two separate numerical simulations. In those simulations, the air domain and the explosives were omitted and ALE algorithm was not used. The predictions are compared with the original fluid-coupled prediction (from Fig. 5). It can be seen that both the fluid-uncoupled predictions by $p_{\text{Int}}^{\text{Def}}$ and $p_{\text{Int}}^{\text{Rigid}}$ have reasonable agreements with the fluid-coupled one before the maximum deflection was attained. Table 6 also tabulates the predicted saturated deflection and the correspond saturation time. In the elastic rebound, there are notable discrepancies between the three curves. Nevertheless for the analysis that focused on the maximum instead of the entire elasto-plastic response (like the present study), the uncoupled loading approach by using either the averaged interface overpressures ($p_{\text{Int}}^{\text{Def}}$ and $p_{\text{Int}}^{\text{Rigid}}$) can yield reasonable prediction of transverse central deflection up to the maximum elasto-plastic response. For simplicity, the loading off the rigid plate, $p_{\text{Int}}^{\text{Rigid}}$, suffices to be served as the loading condition in the subsequent analytical analysis.

4. Analytical model

The dynamic response of the clamped square aluminum plate subjected to a uniformly distributed pulse-pressure (extracted from the preceding FE simulation) will be investigated analytically in this section. For this purpose, the analytical model developed by Yuan and Tan [20] will be modified and used here. The original model in [20] is sufficiently general

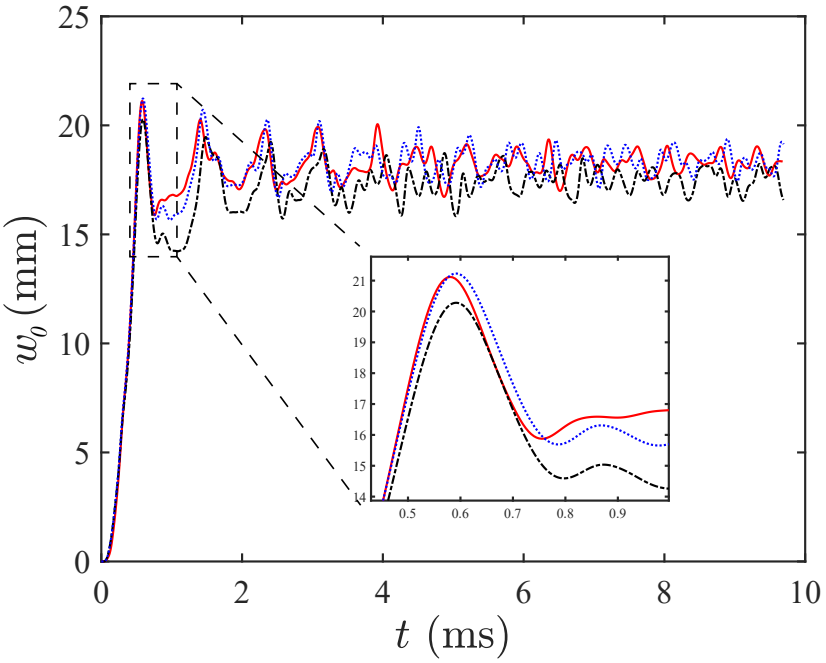

Figure 10: Comparison between the numerical predictions of the aluminum plate's transverse central displacement under different idealised loading conditions. Red line — corresponds to the original numerical prediction in Fig. 5; dotted lines -.-.- (black) and - - - (blue) refer to the uncoupled predictions of w_0 under uniformly distributed pressure of $p_{\text{Int}}^{\text{Rigid}}$ and $p_{\text{Int}}^{\text{Def}}$ respectively.

to deal with deformation and failure of ductile plates to blast loading, which adopts an energy density failure criterion to delineate the various inelastic failure modes (mode I - large inelastic deformation, mode II* - partial tearing, mode II - complete tearing and mode III - transverse shear at the supports); employs the constitutive framework of limit analysis for simplicity; accounts for the simultaneous influence of bending, membrane stretch and transverse shear through an interaction yield criterion; and, include the effects of strain rate on the material flow stress through the Cowper-Symonds relation.

For the current problem that is only concerned with large inelastic deformation, the failure criterion can be omitted for simplification. The effect of transverse shear on interactive yield criterion can also be neglected, since it was shown in [20] that the plastic work absorbed through transverse shear account for less than 5% of the total one in mode I deformation. Despite the aforesaid simplifications, the modified model considers an interactive yield criterion (bending and membrane stretch), travelling plastic hinge lines, the strain-rate sensitivity, and the arbitrary pulse-shape. Notice that only a succinct summary of the modified model will be presented here to avoid considerable overlap to the reference mentioned above. The accuracy of the modified model will be assessed by comparing its predictions against numerical and experimental results.

Table 6: Summary of the numerical simulation results under different loading conditions.

Loading condition	FSI (Y/N)	Saturation time (ms)	Saturated deflection (mm)
8701 Detonation	Y	0.58	21.16
Uniform $p_{\text{Int}}^{\text{Def}}$	N	0.60	21.23
Uniform $p_{\text{Int}}^{\text{Rigid}}$	N	0.60	20.28

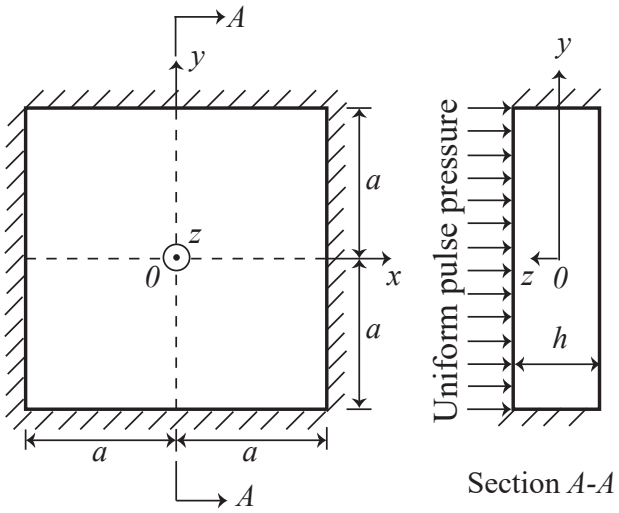

Figure 11: Schematic of a fully clamped square plate (in third-angle projection). Reflectional symmetry exists on two planes: viz. ($x = 0$, $-h/2 \leq z \leq h/2$) and ($y = 0$, $-h/2 \leq z \leq h/2$).

4.1. Problem statement

Consider a fully-clamped square plate of total length $2a$ and thickness h under a uniformly-distributed pulse-pressure $p_{\text{Int}}(t)$ that acts transversely to the x-y plane, as depicted in Fig. 11. Symmetry dictates that only one-quarter of the full plate needs to be modelled. Rigid, perfectly-plastic material (with density ρ and static yield strength σ_0) is used for the current calculation, while elastic deformations are assumed to be negligible for class of problems which is examined in this article. The mean dynamic flow stress of the plate can be estimated according to the Cowper-Symonds constitutive equation [23] as follows

$$\sigma_d = \sigma_0[1 + (\dot{\epsilon}_m/\dot{\epsilon}_0)^{1/q}] \tag{2}$$

where σ_0 is the static yield strength; $\dot{\epsilon}_m$ is the mean uniaxial strain rate; and, $\dot{\epsilon}_0$ and q are material constants.

4.2. Interactive fully plastic stress condition

An interactive fully plastic stress condition combining the bending moment M and membrane force N

$$\frac{|M|}{M_d} + \frac{N^2}{N_d^2} - 1 = 0 \tag{3}$$

is employed to describe the plastic yielding in the plate, where $M_d = \sigma_d H^2/4$ and $N_0 = \sigma_d H$ are the dynamic fully plastic bending moment and in-plane membrane force, respectively. It is convenient to express Eq. 3 in non-dimensional form as follows:

$$|\bar{M}| + \bar{N}^2 - 1 = 0 \tag{4}$$

where $\bar{M} = M/M_d$ and $\bar{N} = N/N_d$ are the non-dimensional fully plastic generalised stresses.

4.3. Equation of motion

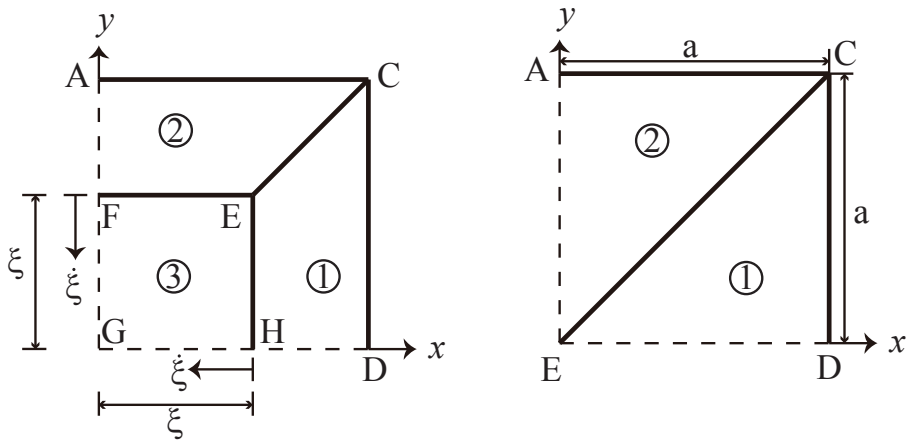

(a) $0 < t \leq t_1$ (b) $t_1 < t \leq t_2$

Figure 12: Deformation mechanism for a quarter of the square plate: (a) Phase I and (b) Phase II.

For a rigid, perfectly plastic plate, travelling plastic hinge lines develop along the principal stress-moment directions. Depending on the position of the travelling hinge line, there are two stages of deformation for a plate (see Fig. 12): (1) plastic hinge lines travel towards the plate's centre; and (2) the plastic hinge lines reach and coalesce at the centre, leading to a final (and stationary) collapse configuration. For the deformation mechanism in Fig. 12a, the transverse velocity profiles in zone ①, ② and ③ for one-quarter of the square plate are

$$\dot{w}_1(x,y,t) = \dot{w}_0(t)(a-x)/[a-\xi(t)], \quad \text{Zone ①} \tag{5a}$$
$$\dot{w}_2(x,y,t) = \dot{w}_0(t)(a-y)/[a-\xi(t)], \quad \text{Zone ②} \tag{5b}$$
$$\dot{w}_3(x,y,t) = \dot{w}_0(t), \quad \text{Zone ③}. \tag{5c}$$

When the travelling plastic hinge line reaches the plate center, i.e. $x = 0$ and $y = 0$, the the transverse velocity profiles for Fig. 12b becomes

$$\dot{w}_1(x,y,t) = \dot{w}_0(t)(a-x)/a, \quad \text{Zone ①} \tag{6a}$$
$$\dot{w}_2(x,y,t) = \dot{w}_0(t)(a-y)/a, \quad \text{Zone ②}. \tag{6b}$$

For both deformation mechanisms, the quarter of the plate's total kinetic energy and strain energy are given, respectively, by

$$T = \frac{1}{2}\rho H\Big[\int_{\xi(t)}^{a}\int_{0}^{\xi(t)} \dot{w}_1^2(x,y,t)\mathrm{d}x\mathrm{d}y + \int_{\xi(t)}^{a}\int_{\xi(t)}^{x} \dot{w}_1^2(x,y,t)\mathrm{d}x\mathrm{d}y + \int_{\xi(t)}^{a}\int_{x}^{a} \dot{w}_2^2(x,y,t)\mathrm{d}x\mathrm{d}y + \int_{0}^{\xi(t)}\int_{\xi(t)}^{a} \dot{w}_2^2(x,y,t)\mathrm{d}x\mathrm{d}y + \int_{0}^{\xi(t)}\int_{0}^{\xi(t)} \dot{w}_3^2(x,y,t)\mathrm{d}x\mathrm{d}y\Big] \quad (7)$$

and

$$\Pi = 2\xi(t)\Big[M_S\theta_1 + Nw_0\theta_1\Big] + 2\int_{\xi(t)}^{a}(M_S + Nw_1)\theta_1 + \sqrt{2}\int_{\xi(t)}^{a}[M_S + Nw_1]\theta_3\mathrm{d}x + \xi(t)(2\theta_1 + 2\theta_2)(M_P + Nw_3) \quad (8)$$

where $\theta_1 = \theta_2 = w_0(t)/[a - \xi(t)]$ are relative rotations along the outer boundaries (fully clamped) of plastic zone ① and ② respectively; and $\theta_3 = \sqrt{2}\theta_1$ is the change in rotation across the inclined plastic hinges that lie at the intersections of plastic zone ① and ②. Note that the sum of the first two terms in Eq. 8 corresponds to the strain energy dissipated along its support, whereas the last term relates to the strain energy absorbed at the plate interior.

The parameters M_S, Q_S, N, M_P and $\xi(t)$ in Eqs. 7 and 8 are unknowns. Recasting them in non-dimensional form, viz. $\bar{M}_S$, $\bar{Q}_S$, $\bar{N}$, $\bar{M}_P$ and $\bar{\xi} = \xi(t)/a$, they are calculated as described below.

The non-dimensional position of the travelling plastic hinge line is

$$\bar{\xi} = \int_0^t \dot{\bar{\xi}}\mathrm{d}t \quad (9)$$

and $\dot{\bar{\xi}}$ is the non-dimensional velocity of the travelling plastic hinge line given by

$$\dot{\bar{\xi}} = \frac{(\sigma_d/\rho a^2)\Big[12(\bar{M}_S + \bar{M}_P) + 24\bar{N}\Delta\bar{w}_0(1+\bar{\xi})\Big]}{(\bar{\xi}-1)(1+3\bar{\xi})\bar{I}} \quad (10)$$

where $\bar{w}_0 = w_0(t)/h$ and $\bar{I} = \int_0^t p(t)/(\rho h^2)\mathrm{d}t$. When the travelling plastic hinge lines EF and EH reach the centre of the plate, they coalesce with the plastic hinge line CE into a single plastic hinge line so that in the subsequent motion,

$$\dot{\bar{\xi}} = 0 \quad \text{and} \quad \bar{\xi} = 0. \quad (11)$$

The generalised strain rates associated with bending $\dot{\theta}_S$ and membrane $\dot{\bar{\Delta}}$ are given by

$$\dot{\theta}_S = \frac{\dot{\bar{w}}_0}{\eta(1-\bar{\xi})} \quad (12a)$$

$$\dot{\bar{\Delta}} = \frac{\dot{\Delta}}{h} = \frac{\bar{w}_0\dot{\bar{w}}_0}{\eta(1-\bar{\xi})} \quad (12b)$$

where $\eta = a/h$. Normality requirements dictate that [23]

$$\frac{\dot{\bar{\Delta}}}{\dot{\theta}_S} = \frac{1}{2}\bar{N} \tag{13}$$

Substituting Eqs. 12 into 13, and re-arranging, gives

$$\bar{N} = 2\bar{w}_0 \tag{14}$$

if $\bar{M}_S > 0$, and

$$\bar{N} = 1 \tag{15}$$

if $\bar{M}_S = 0$.

Since the *Lagrangian* of the quarter plate is

$$\mathcal{L} = T + \Pi, \tag{16}$$

the differential equation governing w_0 is obtained by substituting Eqs. 16, 7 and 8 into the well-known Lagrange equation of the 2nd kind

$$\frac{\mathrm{d}}{\mathrm{d}t}\left(\frac{\partial \mathcal{L}}{\partial \dot{w}_0}\right) + \frac{\partial \mathcal{L}}{\partial w_0} = Q_0 \tag{17}$$

where the generalised force Q_0 is expressed as

$$Q_0 = p_{\mathrm{Int}}(t) \int_0^a \int_0^a w(x,y)/w_0 \mathrm{d}x\mathrm{d}y. \tag{18}$$

The temporal evolution of w_0 is obtained by solving the aforementioned equations using the 4th order Runge-Kutta method with the initial conditions of $\bar{w}_0 = \dot{\bar{w}}_0 = 0$. Plate deformation ends at time $t = t_{\mathrm{Sat}}$ if the motion of the plate ceases, i.e.

$$\dot{\bar{w}}_0 = 0. \tag{19}$$

To incorporate the strain rate sensitivity effect, the mean strain rate $\dot{\epsilon}_m$ and dynamic yield strength σ_d (in Eq. 2) need to be obtained based on a first round of prediction (after solving Eq. 17 with the static yield strength, $\sigma_d = \sigma_0$) without the strain-rate effect. The strain rate for a square plate can be estimated as [23, 29]

$$\dot{\epsilon} = \frac{\bar{w}_0 \dot{\bar{w}}_0}{4\eta^2}. \tag{20}$$

The mean strain rate $\dot{\epsilon}_m$ is obtained by averaging the strain rate $\dot{\epsilon}$ during the entire response $0 \leq t \leq t = t_{\mathrm{Sat}}$. The equation of motion (Eq. 17) is then solved again using the dynamic yield strength σ_d.

The saturated impulse is obtained by integrating the interface pressure with time up to the saturation time given by:

$$I_{\mathrm{Sat}} = \int_0^{t_{\mathrm{Sat}}} p_{\mathrm{Int}}(t)dt. \tag{21}$$

The saturated deflection is the plastic deformation of the plate at time $t = t_{\mathrm{Sat}}$ as follows:

$$w_{\mathrm{Sat}} = w_0(t = t_{\mathrm{Sat}}). \tag{22}$$

4.4. Validations

Figure 13 compares the analytical prediction, numerical prediction and DIC measurements of the aluminum plate's transverse central deflection under the confined blast loading. The time-history of the pulse pressure in the analytical model, viz. $p_{\mathrm{Int}}^{\mathrm{Rigid}}$, is also plotted in Fig. 13. There are reasonable agreements between the analytical predictions and the experimental results. The predicted saturated deflection and saturation time are in excellent agreement with the experimental counterparts (as seen in Table 1).

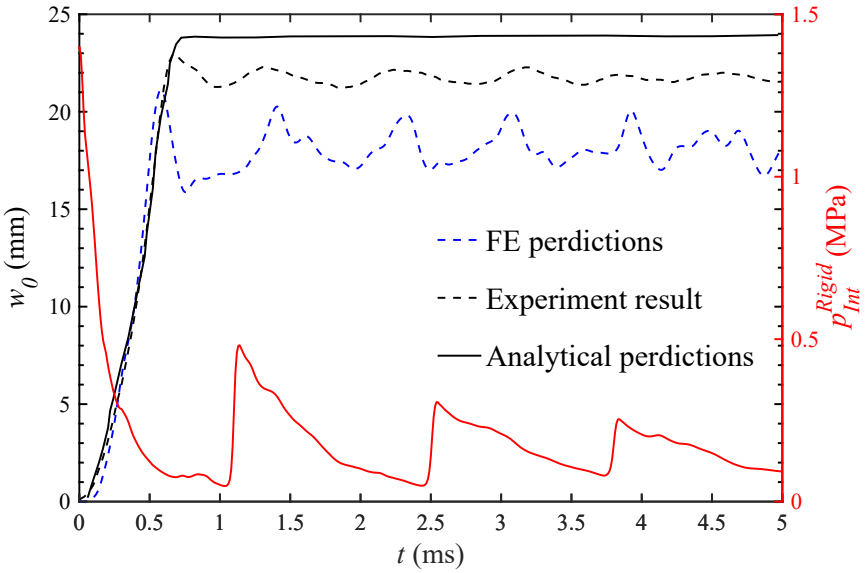

Figure 13: Comparison of the analytical temporal central deflection (—) with numerical (-.-) and experimental data (- - -). Red line — refers to the average interface overpressure off the rigid plate $p_{\mathrm{Int}}^{\mathrm{Rigid}}$ (FE).

5. Parametric studies

The current experiment only investigated a specific problem of a square metal plate under an internal blast loading. The standoff distance and the confinement geometry can have huge impacts on the blast response of the metal structure, and in turn the outcomes of the saturation phenomenon. The validated analytical model will be used in this section to

carry out parametric studies to elucidate the effect of standoff distance and the confinement geometry upon the saturated deflection, saturation time and saturated impulse for square steel plates. In the parametric studies, material properties, charge type and mass remain the same as those investigated in the previous sections. The pulse pressure is idealised by an equivalent uniformly distributed pulse pressure from the rigid plate's surface. The transverse central deflections of the aluminum plate subjected to the pulse pressure are then predicted by the current analytical model, and will be compared against numerical predictions considering the effect of FSI.

5.1. The effect of standoff distance

Table 7: Simulation plan of the first parametric study.

Test no.	Half width L (mm)	Thickness H (mm)	L/H	Plate mass (kg)	Standoff distance (mm)	Charge mass (g)
1	150	2	75	0.49	100	10
2	150	2	75	0.49	200	10
3	150	2	75	0.49	300	10
4	150	2	75	0.49	500	10
5	150	2	75	0.49	600	10
6	150	2	75	0.49	700	10

The details of the simulation plan for the first parametric study are shown in Table. 7. Figure 14 compares the analytical and FE predictions of the transient central deflection at different standoff distance R. The case of $R = 400$ mm was omitted since it has been shown previously in Fig. 13. Notice that in the FE predictions, the fluid was coupled with the structural response, and the ALE algorithm was used. The time history of the uncoupled average interface overpressure $p_{\text{Int}}^{\text{Rigid}}$ is also inserted in the figure. It can be seen that detonating the explosive at various locations would yield pulse pressure with a wide range of pulse-shapes and peak overpressure. Despite these complex loading conditions, the analytical predictions of w_0 agree well with the numerical counterparts, showcasing the efficacy of the current methodology in assessing the consequence of internal blast upon the ductile plate in different loading scenarios.

Figures 15a - 15d focus on the key response quantities, viz. saturated deflection w_{Sat}, saturation time t_{Sat}, peak overpressure p_{Int}^{m} and saturated impulse I_{Sat} from the results in Figs. 14. It is evident that the current analytical model slightly overpredicts the w_{Sat} compared to the numerical ones. As mentioned earlier, this is because the analytical model neglected the effect of linear hardening in its constitutive behaviour. As a consequence, the analytical prediction of t_{Sat} is also greater than the numerical counterparts (since the time for plate motion to cease is longer for the more severely deformed plate predicted by the analytical model). The analytical model successfully predicts the trend of w_{Sat} with increasing R, which increases monotonically with R despite the notable case of $R =$

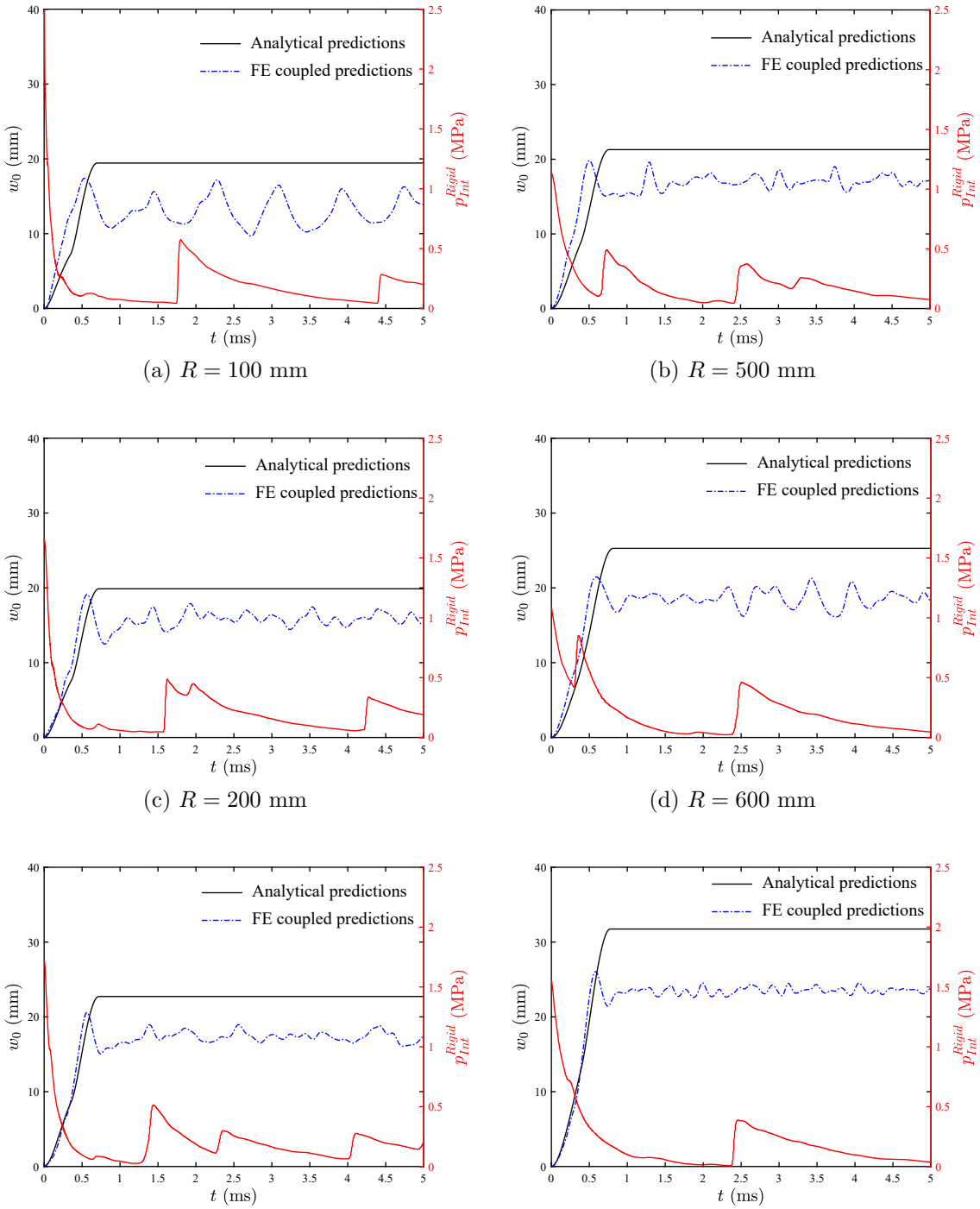

(a) $R = 100$ mm (b) $R = 500$ mm

(c) $R = 200$ mm (d) $R = 600$ mm

(e) $R = 300$ mm (f) $R = 700$ mm

Figure 14: Predictions of central deflection w_0 (FE -.-.- and analytical —) and average interface overpressure off the rigid plate $p_{\text{Int}}^{\text{Rigid}}$ (FE — at different standoff distance R.

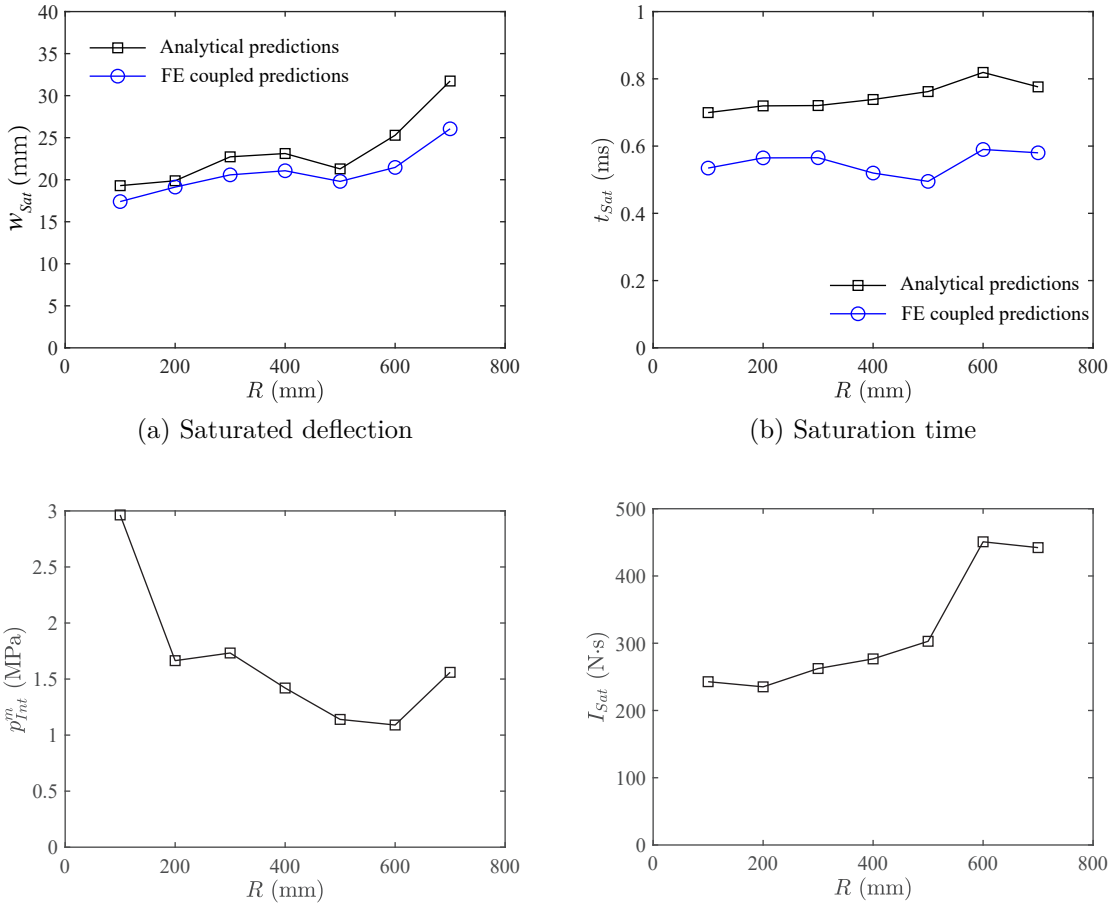

(a) Saturated deflection

(b) Saturation time

(c) Maximum average interface overpressure

(d) Saturated impulse

Figure 15: Summaries of the key physical quantities (associated with loading, impulse and deflection) in the parametric study for different standoff distances R: (a) saturated deflection, w_{Sat}, (b) saturation time t_{Sat}, (c) maximum average interface overpressure p^m_{Int} and (d) saturated impulse I_{Sat}.

500 mm. The explanation for the effect of standoff distance in internal blast loading was comprehensive in [15] and will not be duplicated here.

Figure 15 show that although t_{Sat} is not sensitive to R, the peak overpressure p^m_{Int} and the saturated impulse I_{Sat} is strongly influence by it. It is surprising to note that the saturated deflection w_{Sat} is not strictly proportional to the saturated impulse I_{Sat} when comparing the case of $R = 600$ and $R = 700$ mm. This contradicts to the findings in the saturation analysis of [19] where a rectangular pulse was used as loading condition. The former case, though under greater saturated impulse, displays less deformation. This can be explained by revisiting the transient predictions in Figs. 14d and 14f. Although the case of $R = 600$ mm has greater I_{Sat}, a large proportion of it (after the second peak of interface overpressure) is transmitted after the plate has developed considerable deflection. Due to the membrane effect, the structure has been strengthened and is less prone to deflect in the ensuing loading.

In this case, the saturated impulse for $R = 600$ mm is somehow offset by the enhanced structural resistance from the membrane effect. Unlike the pulse shape for $R = 600$ mm, the average interface overpressure of $R = 700$ mm decays monotonically with time. In this case, the majority of the impulse was imparted to the plate before the development of large deflection. In light of the above, both the complex pulse shape and saturated impulse need to be considered when assessing the plate's maximum response to internal blast loadings.

5.2. The effect of confinement geometry

Table 8: Simulation plan of the second parametric study.

Test no.	Half width L (mm)	Thickness H (mm)	L/H (mm)	Plate mass (kg)	Standoff distance (mm)	Charge mass (g)
1	100	4.50	22.2	0.49	400	10
2	125	2.88	43.1	0.49	400	10
3	175	1.47	119.0	0.49	400	10
4	200	1.13	177.0	0.49	400	10

In the second parametric study, the effect of the confinement geometry of the blast chamber was investigated. The opening area was varied while the length of the blast chamber remained the same as the test rig in the current experiment. In such a case, the exposed area of the plate needs to change in accordance with the opening area of the blast chamber. The thickness of the target plate was adjusted such that the plate's mass remained the same for each variation. The details of this parametric study were tabulated in Table 8.

Figures 16a-16d plot the analytical and numerical predictions of transient central deflection for half-width to thickness ratio L/H ranging from 22.2 to 177, where reasonable agreements can be seen. The summary of the four simulations is plotted in Figs. 17a-17d, including maximum deflection, saturation time, peak overpressure, and saturated impulse. It can be seen that the current analytical model successfully predicted the trend of L/H with saturated deflection w_{Sat} and saturation time t_{Sat} when compared to the numerical predictions. Again, both the analytical predictions of w_{Sat} and t_{Sat} are higher than the numerical one. Figures 17c and 17d also indicate that the peak average interface overpressure and saturated impulse reduce monotonically with L/H. This may be due to the fact that the loading area increases considerably with L/H leading to a significant drop of the *average* interface pressure and impulse under the blast loading resulting from the detonation of the same charge mass.

6. Conclusion

A combined experimental, numerical and analytical investigation was carried out to study the impulse saturation phenomenon in internal blast loaded ductile plates. The transient central deflection was measured in the experiment, which validates the numerical and analytical predictions. A methodology was put forward to idealise the spatial internal blast loading

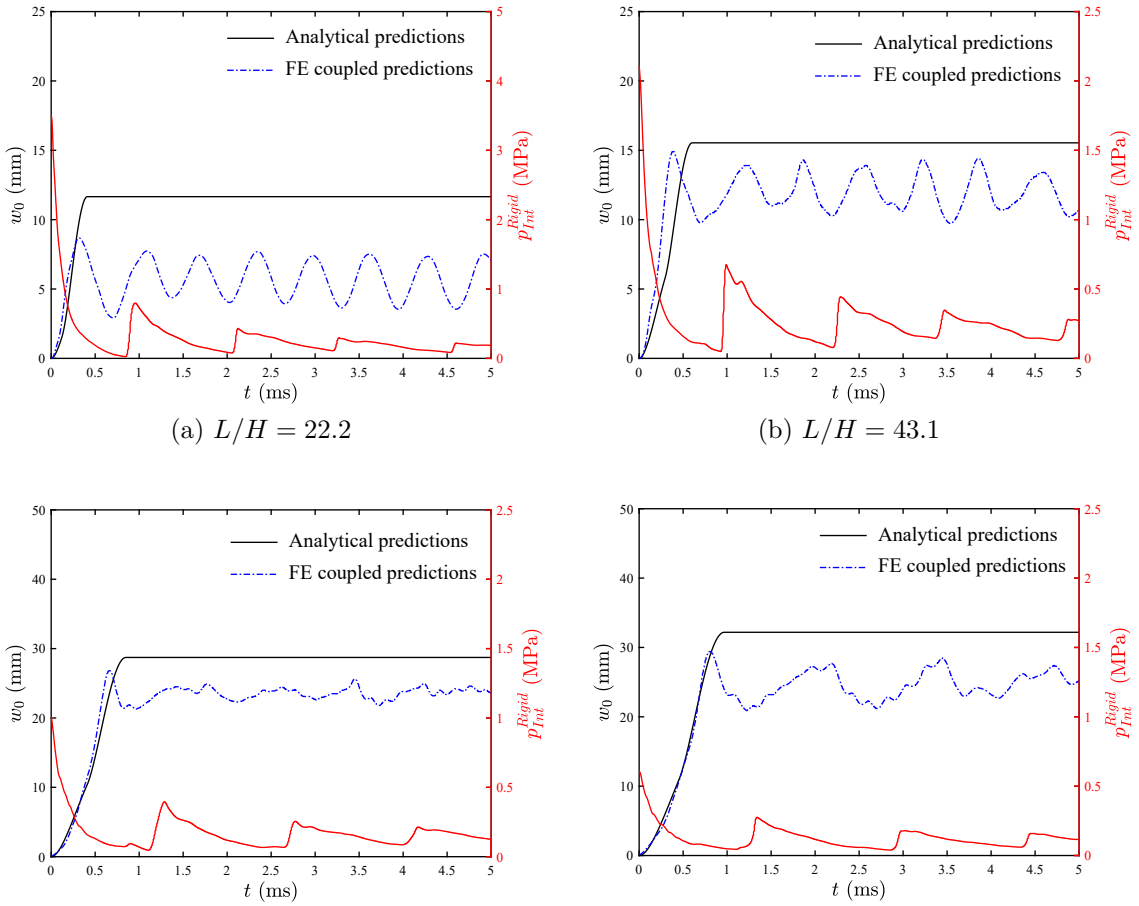

(a) $L/H = 22.2$ (b) $L/H = 43.1$

(c) $L/H = 119$ (d) $L/H = 177$

Figure 16: Predictions of central deflection w_0 (FE -.-.- and analytical —) and average interface overpressure off rigid plate $p_{\text{Int}}^{\text{Rigid}}$ (FE) — for different L/H.

as a uniformly distributed pulse pressure with conserved total impulse. An analytical model was developed to quickly predict fully-clamped square ductile plate under pulse-pressure with arbitrary pulse shape and significant pulse duration with reasonable fidelity.

The analytical model was then employed to investigate the effect of standoff distance and confinement geometry upon the saturation time, saturated impulse and deflection of square metal plates through parametric studies. It was found that (1) both peak average interface overpressure and saturated impulse do not increase monotonically with standoff distance, (2) the maximum deflection may not be proportional to the saturated impulse; and (3) the maximum deflection and saturated impulse respectively have positive and negative correlations with the confinement opening width. While finding (1) agree with the finding in the authors' recent study [15], finding (2) contradicts with the findings from existing saturation analysis for unconfined air blasts [19]. The contradiction with the existing findings may be due to the difference in pulse shape, i.e. a rectangular pulse was used in [19]. This highlights

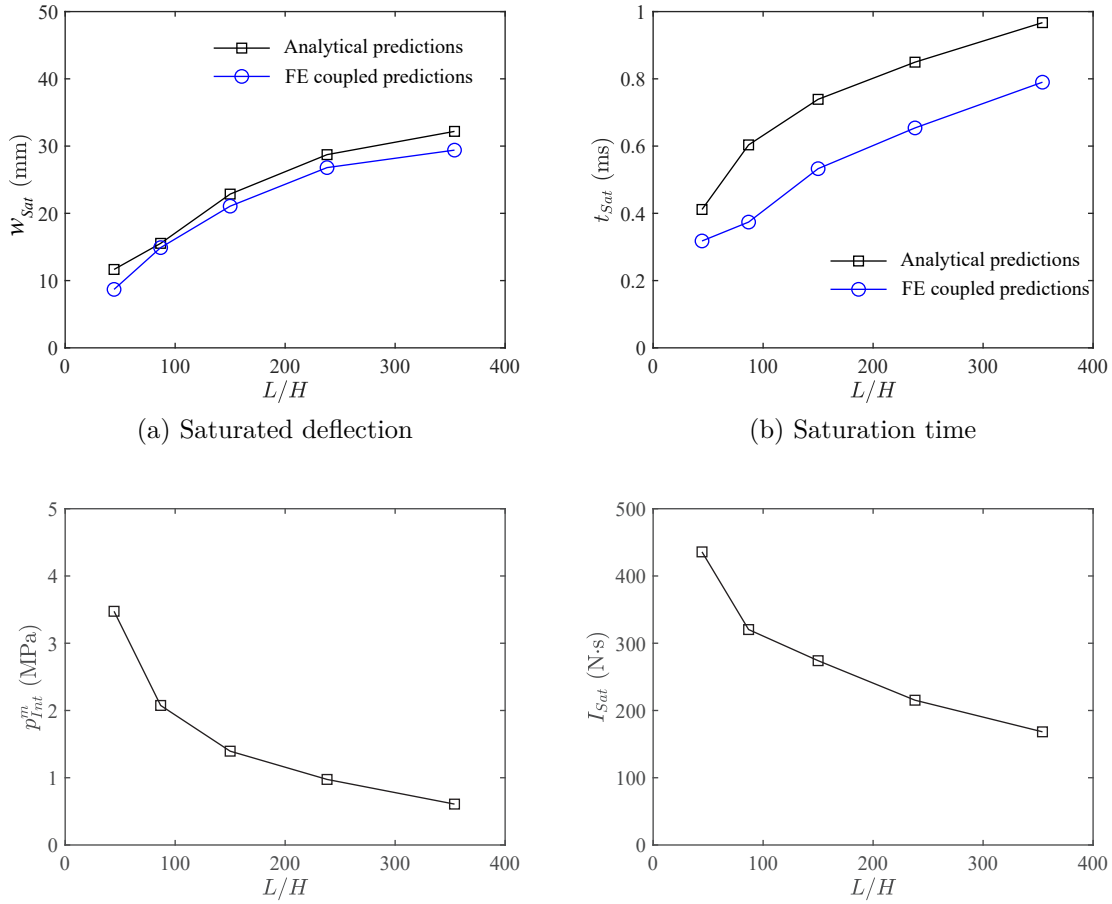

(a) Saturated deflection

(b) Saturation time

(c) Maximum average interface overpressure

(d) Saturated impulse

Figure 17: Summaries of the key physical quantities (associated with loading, impulse and deflection) in the parametric study for different L/H: (a) saturated deflection, w_{Sat}, (b) saturation time t_{Sat}, (c) maximum average interface overpressure p^m_{Int} and (d) saturated impulse I_{Sat}.

the complex nature of the structural response under internal blast loadings and the importance to consider both the saturated impulse and pulse shape to estimate the structural response.

The parametric studies in the current work only dealt with the effect of standoff distance and confinement opening geometry, but did not explore the other important aspects, e.g. the target's material properties, confinement length, the extent of venting, explosive mass, to name a few. Notwithstanding, the proposed models lay an important theoretical framework to investigate how can the aforesaid in part, or in combination, affect the impulse saturation of internal blast loaded metal structures in future studies.

Acknowledgment

This research was financially supported by the National Science Foundation of China under Grant No. 12102049 and the State Key Laboratory of Explosion Science and Technology, Beijing Institute of Technology under Grant No. QNKT22-02.

References

[1] Karagiozova, D., Alves, M., On the saturated impulse for a circular hollow beam under pressure pulse loading, International Journal of Impact Engineering (2021) 103958.

[2] Tian, L., Chen, F., Zhu, L., Yu, T. X., Large deformation of square plates under pulse loading by combined saturation analysis and membrane factor methods, International Journal of Impact Engineering 140 (2020) 103546.

[3] Yuan, Y., Zhu, L., Bai, X., Yu, T. X., Li, Y., Tan, P. J., Pressure-impulse diagrams for elastoplastic beams subjected to pulse-pressure loading, International Journal of Solids and Structures 160 (2019) 148–157.

[4] Jones, N., Slamming damage., Journal of Ship Research (17) (1973) 80–6.

[5] Zhao, Y. P., Yu, T. X., Fang, J., Large dynamic plastic deflection of a simply supportedbeam subjected to rectangular pressure pulse, Struct Eng Mech 3 (6) (1994) 583–92.

[6] Zhao, Y. P., Yu, T. X., Fang, J., Saturation impulses for dynamically loaded structures with finite-deflections, Arch Appl Mech 64 (3) (1995) 223–32.

[7] Bai, X., Zhu, L., Yu, T. X., Saturated impulse for pulse-loaded rectangular plates with various boundary conditions, Thin-Walled Structures 119 (2017) 166–177.

[8] Zhu, L., He, X., Chen, F. L., Bai, X., Effects of the strain rate sensitivity and strainhardening on the saturated impulse of plates, Lat Am J Solids Struct 14 (7) (2017) 1273–92.

[9] Zhu, L., Tian, L., Chen, F., Yu, T. X., A new equivalent method for complex-shaped pulse loading based on saturation analysis and membrane factor method, International Journal of Impact Engineering 158 (2021) 104018.

[10] Yuan, Y., Tan, P. J., Shojaei, K. A., Wrobel, P., Large deformation, damage evolution and failure of ductile structures to pulse-pressure loading, Int. J. Solids Struct. 96 (2016) 320 – 339.

[11] Edri, I., Savir, Z., Feldgun, V., Karinski, Y., Yankelevsky, D., On blast pressure analysis due to a partially confined explosion: I. experimental studies, International Journal of Protective Structures 2 (1) (2011) 1–20.

[12] Feldgun, V. R., Karinski, Y. S., Edri, I., Yankelevsky, D. Z., Prediction of the quasi-static pressure in confined and partially confined explosions and its application to blast response simulation of flexible structures, International Journal of Impact Engineering 90 (2016) 46–60.

[13] Pickerd, V., Bornstein, H., McCarthy, P., Buckland, M., Analysis of the structural response and failure of containers subjected to internal blast loading, International Journal of Impact Engineering 95 (2016) 40–53.

[14] Zheng, C., Kong, X., Wu, W., Xu, S., Guan, Z., Experimental and numerical studies on the dynamic response of steel plates subjected to confined blast loading, International Journal of Impact Engineering 113 (2018) 144–160.

[15] Yuan, Y., Zhang, C., Xu, Y., Influence of standoff distance on the deformation of square steel plates subjected to internal blast loadings, Thin-Walled Structures 164 (2021) 107914.

[16] Langdon, G. S., Kriek, S., Nurick, G. N., Influence of venting on the response of scaled aircraft luggage containers subjected to internal blast loading, International Journal of Impact Engineering 141 (2020) 103567.

[17] Zhang, C., Tan, P. J., Yuan, Y., Confined blast loading of steel plates with and without pre-formed holes, International Journal of Impact Engineering 163 (2022) 104183.

[18] Geretto, C., Chung Kim Yuen, S., Nurick, G. N., An experimental study of the effects of degrees of

confinement on the response of square mild steel plates subjected to blast loading, International Journal of Impact Engineering 79 (2015) 32–44.
[19] Tian, L., Chen, F. L., Zhu, L., Yu, T. X., Saturated analysis of pulse-loaded beams based on Membrane Factor Method, International Journal of Impact Engineering 131 (2019) 17–26.
[20] Yuan, Y., Tan, P. J., On large deformation, damage and failure of ductile plates to blast loading, International Journal of Impact Engineering 132 (2019) 103330.
[21] Aune, V., Fagerholt, E., Hauge, K., Langseth, M., Borvik, T., Experimental study on the response of thin aluminium and steel plates subjected to airblast loading, International Journal of Impact Engineering 90 (2016) 106–121.
[22] Kong, X., Wang, X., Zheng, C., Xu, J., Li, Y., Wu, W., Experimental and numerical investigations of dynamic response and failure of fluid-filled container under blast loadings from a cased charge, Composite Structures 227 (2019) 111339.
[23] Jones, N., Structural Impact, Cambridge: Cambridge University Press, 1989.
[24] Johnson, G. R., Cook, W. H., A constitutive model and data for metals subjected to large strains, high strain rates and high temperatures, The 7th International Symposium on Ballistics.
[25] Deng, Y., Zhang, Y., Xiao, X., Hu, A., Wu, H., Xiong, J., Experimental and numerical study on the ballistic impact behavior of 6061-T651 aluminum alloy thick plates against blunt-nosed projectiles, International Journal of Impact Engineering 144 (2020) 103659.
[26] Yuan, Y., Tan, P. J., Shojaei, K. A., Wrobel, P., On momentum transfer and external work done to clamped elasto-plastic beams in an air blast, International Journal of Mechanical Sciences 146-147 (2018) 377–385.
[27] Hutchinson, J. W., Energy and momentum transfer in air shocks, J. Appl. Mech. 76 (5) (2009) 051307–051307.
[28] Subramaniam, K. V., Nian, W., Andreopoulos, Y., Blast response simulation of an elastic structure: Evaluation of the fluid structure interaction effect, International Journal of Impact Engineering 36 (7) (2009) 965 – 974.
[29] Zhu, L., Xu, H., Chen, F. L., Bai, X., Effects of the strain rate sensitivity and strainhardening on the saturated impulse of plates, Latin American Journal of Solids and Structures (14) (2017) 1273–1292.